Remote Sensing of Environment 180 (2016) 154–163

Contents lists available at ScienceDirect

Remote Sensing of Environment

journal homepage: www.elsevier.com/locate/rse

Reduced ascending/descending pass bias in SMOS salinity data demonstrated by observing westward-propagating features in the South Indian Ocean

Christopher J. Banks [a,*], Meric A. Srokosz [a], Paolo Cipollini [a], Helen M. Snaith [b], Jeffrey R. Blundell [c], Christine P. Gommenginger [a], Eleni Tzortzi [a,1]

[a] National Oceanography Centre, European Way, Southampton SO14 3ZH, United Kingdom
[b] British Oceanographic Data Centre, National Oceanography Centre, European Way, Southampton, SO14 3ZH, United Kingdom
[c] Ocean and Earth Science, National Oceanography Centre Southampton, University of Southampton, SO14 3ZH, United Kingdom

ARTICLE INFO

Article history:
Received 21 July 2015
Received in revised form 21 December 2015
Accepted 17 February 2016
Available online 3 March 2016

Keywords:
Ocean salinity
Rossby wave
Planetary wave
Soil moisture and ocean salinity satellite
SMOS
Indian Ocean
Sea surface salinity
Salinity anomaly

ABSTRACT

The European Space Agency (ESA) Soil Moisture and Ocean Salinity (SMOS) satellite has been providing data, including sea surface salinity (SSS) measurements, for more than five years. However, the operational ESA Level 2 SSS data are known to have significant spatially and temporally varying biases between measurements from ascending passes (SSS_A) and measurements from descending passes (SSS_D).

This paper demonstrates how these biases are reduced through the use of SSS anomalies. Climatology products are constructed using SMOS Level 2 data to provide daily, one-degree by one-degree climatologies separately for ascending and descending passes using a moving window approach (in time and space). The daily, one-degree products can then be averaged to provide values of climatological SSS at different spatial and/or temporal resolutions.

The averaged values of the SMOS climatology products are in good general agreement with data from the World Ocean Atlas 2013. However, there are significant differences at high latitudes, as well as in coastal and dynamic regions, as found by previous studies. Both the mean and standard deviation of the differences between data from ascending passes and data from descending passes for the anomalies are reduced compared with those obtained using the original salinity values.

Geophysical signals are clearly visible in the anomaly products and an example is shown in the Southern Indian Ocean of westward-propagating signals that we conclude represent the surface expression of Rossby waves or large-scale non-linear eddies. The signals seen in salinity data agree (in speed) with those from sea surface temperature and sea surface height and are consistent with previous studies.

© 2016 The Authors. Published by Elsevier Inc. This is an open access article under the CC BY license (http://creativecommons.org/licenses/by/4.0/).

1. Introduction

Sea surface salinity (SSS) is an essential climate variable (GCOS, 2011) and critical to our understanding of ocean circulation and the global water cycle. The launch of the European Space Agency (ESA) Soil Moisture and Ocean Salinity (SMOS) satellite in November 2009 was a landmark in satellite oceanography enabling the routine monitoring of SSS on synoptic scales. Historically, measurements of SSS were relatively sparse, as they were limited to in situ measurements from ships, drifters and moorings. Since the turn of the century, the situation has markedly improved due to the growth of the Argo profiling buoy system (Gould et al., 2004; http://www.argo.ucsd.edu; http://argo.jcommops.org). However, there are still large areas of the global oceans with limited or no in situ measurements of SSS.

The utility of SSS data from SMOS for scientific exploitation has been demonstrated for a variety of locations and uses, for example: the relationship of rainfall rate and SSS (Boutin et al., 2014; although the relationship is problematic); monitoring of large, freshwater river plumes (Grodsky et al., 2012; Fournier, Chapron, Salisbury, Vandemark, & Reul, 2015); tropical salinity variability (Tzortzi, Josey, Srokosz, & Gommenginger, 2013); observation of tropical instability wave signals in the equatorial Pacific Ocean (Yin et al., 2014b); and the study of mesoscale features in the Gulf Stream (Reul et al., 2014).

However, it has been shown (e.g. Banks, Gommenginger, Srokosz, & Snaith, 2012) that the ESA SSS data have significant temporally varying

* Corresponding author.
E-mail addresses: chris.banks@noc.ac.uk (C.J. Banks), mas@noc.ac.uk (M.A. Srokosz), cipo@noc.ac.uk (P. Cipollini), hms@bodc.ac.uk (H.M. Snaith), jeff@noc.soton.ac.uk (J.R. Blundell), cg1@noc.ac.uk (C.P. Gommenginger), e.tzortzi@exeter.ac.uk (E. Tzortzi).
[1] Now at: Exeter Climate Systems, Department of Mathematics, University of Exeter, Streatham Campus, Levar Building, North Park Road, EX4 4QF, Exeter, United Kingdom.

http://dx.doi.org/10.1016/j.rse.2016.02.035
0034-4257/© 2016 The Authors. Published by Elsevier Inc. This is an open access article under the CC BY license (http://creativecommons.org/licenses/by/4.0/).

biases between measurements from ascending passes (SSS_A) and measurements from descending passes (SSS_D; see Section 2.1.1 below, regarding Aquarius problems). This paper will demonstrate a methodology for reducing these variable biases in the open ocean through the use of SSS anomalies based on data only from SMOS. These anomaly products are well-suited to observing oceanographic processes: as an example we show evidence of westward propagating signals in the South Indian Ocean (SIO), which represent the surface expression of Rossby waves or large-scale non-linear eddies.

Rossby, or planetary, waves are important in oceanography as, amongst other impacts, they are involved in the setup and perpetuation of western boundary currents (Killworth, Chelton, & DeSzoeke, 1997). Typically Rossby waves have speeds of a few centimetres per second and their speed increases as the latitude approaches the equator, they are linear (i.e. their propagation speed does not depend on amplitude) and do not transport water. Before the advent of satellite measurements of sea surface height (SSH) an indirect confirmation of the existence of planetary waves in the ocean had only been possible from sparse in situ measurements. Signals attributed to Rossby waves have now been fully observed and characterized in satellite-derived fields of SSH from altimetry (e.g. Chelton & Schlax, 1996), sea surface temperature (SST; Hill, Robinson, & Cipollini, 2000) and chlorophyll-a (e.g. Cipollini, Cromwell, Challenor, & Raffaglio, 2001; Killworth, Cipollini, Uz, & Blundell, 2004). Thanks to the increased resolution afforded by merging multiple altimetric missions, Chelton, Gaube, Schlax, Early, and Samelson (2011a); Chelton, Schlax, and Samelson (2011b) have been able to revisit the observations in SSH and chlorophyll and showed that at mesoscale wavelengths (<300 km) the signals are dominated by non-linear eddies, which transport water in their interior. Note that at large length scales eddies and Rossby waves have the same propagation speeds. Rossby waves remain dynamically important at the larger scales, and in recent years, with the ability to measure SSS from space, a number of studies have considered the potential for observing Rossby wave signals in salinity. Both Heffner, Subrahmanyam, and Shriver (2008) and Subrahmanyam, Heffner, Cromwell, and Shriver (2009) have calculated Rossby wave speeds in the SIO based on output from the Hybrid Coordinate Ocean Model (HYCOM; http://hycom.org/). Both studies show an equatorwards increase in Rossby wave speeds from 30°S to about 10°S (~5 cm/s to 23 cm/s), in agreement with theoretical mode 1 Rossby wave speeds based on Killworth and Blundell (2003a, 2003b). More recently, Menezes, Vianna, and Phillips (2014) have concluded that Rossby waves are visible using, amongst other data sources, two years of data from the NASA/CONAE Aquarius satellite (V2.0 of the Combined Active Passive data product; Yueh, 2013; Yueh et al., 2013) in the SIO between 15°S and 28°S.

Further details about the SMOS satellite and the ascending/descending bias are given in Section 2. This is followed in Section 3 by: an explanation of the data used in the study; details of the three study regions used for assessing the reduction in open ocean bias as a result of using the anomaly approach (one in the North Atlantic, another in the South pacific and the third in the South Indian Ocean). A fourth area is introduced, also in the South Indian Ocean, where the Rossby wave investigations are undertaken. Section 3 also provides details of the processing of SMOS data (SSS and auxiliary SST) and of the sea surface height anomaly (SSHA) data used for comparisons of the speeds of the propagating features. The bias reduction method is described in Section 4, followed by the results and discussion in Section 5. Finally, Section 6 gives the conclusions of the study.

2. SMOS mission

The use of passive microwave for measuring salinity from space has been considered for many years. However, as discussed by Swift (1980) the size of the antenna needed to achieve adequate spatial resolution was prohibitive for deployment on a spacecraft. SMOS measures salinity using L-band (1.413 GHz; 21 cm) utilizing an innovative, two-dimensional interferometric radiometer (swath ~1000 km) (Mecklenburg et al., 2012).

The oceanographic requirements for the accuracy of SMOS SSS are based on the scientific requirements defined by GODAE (Global Ocean Data Assimilation Experiment) i.e. 0.1 pss (practical salinity scale) accuracy averaged over periods of 10–30 days and 1°–2° (100–200 km) spatial extent. To meet these requirements, individual measurements (Level 2; L2) from SMOS need spatio-temporal averaging to provide gridded Level 3 (L3) data products.

The instrument on-board SMOS is the Microwave Imaging Radiometer using Aperture Synthesis (MIRAS; Brown, Torres, Corbella, & Colliander, 2008). MIRAS comprises 69 receivers distributed over three Y-shaped arms and a larger antenna is synthesized through multiple cross-correlations between pairs of receivers. All L2 data are mapped onto the hexagonal ISEA (Icosahedron Snyder Equal Area) grid (Suess, Matos, Gutierrez, Zundo, & Martin-Neira, 2004). With a revisit period of 3-days SMOS provides data on SSS (or soil moisture) over the entire globe (Mecklenburg et al., 2012) with an average radiometer resolution ~40 km.

There are still unknowns regarding the effects of surface roughness on measured brightness temperature (T_B) at L-band. The ESA L2 SMOS SSS products provide results based on three different forward models (SMOS Team, 2010) whereas the NASA/CONAE Aquarius mission employs a further model (Wentz & Le Vine, 2011). However, for the purposes of this study only SMOS Model 1, a theoretical model based on the two-scale scattering approximation (Yueh, 1997), is used. Previous work (Banks et al., 2012) has shown that the differences amongst SSS estimates obtained from the three SMOS models are significantly less than differences due to other factors (e.g. satellite travel direction, wind speed).

2.1. Known issues

2.1.1. Ascending versus descending bias

As mentioned above, and in spite of extensive work, there remain significant issues affecting the performance of SMOS in retrieving salinity, in particular related to the satellite direction of travel. SMOS has a sun-synchronous orbit such that at ~6 a.m. local time SMOS is ascending (satellite moving from south to north) and at ~6 p.m. is descending (satellite moving north to south). Comparisons between SSS from ascending passes and SSS from descending passes clearly show SMOS displays temporally varying (seasonal) biases. Many authors (e.g. Tenerelli, Reul, Mouche, & Chapron, 2008) have linked these biases to imperfect corrections in the processor (e.g. for galactic glint). One approach to dealing with this is to calibrate to another SSS data source and this is the approach for the CATDS-CEC-IFREMER L3 Product (http://www.catds.fr/) using a daily adjustment to climatology over a large area (~10°×10°). The Aquarius satellite, operating at the same frequency as SMOS, also has an issue with bias between SSS_A and SSS_D although the magnitude is significantly lower (e.g. Lagerloef, Kao, Meissner, & Vazquez, 2015).

2.1.2. Other issues

Although L-band is a protected frequency, the problem of radio frequency interference (RFI) has been, and remains, a serious concern for the retrieval of salinity from space. Since the launch of SMOS much work has been undertaken to minimize the impacts of RFI on the quality of measured T_B from L-band sensors (e.g. ESA Earth Observation Programme Board, 2011; Oliva, Nieto, & Felix-Redondo, 2013; Soldo et al., 2014). The ESA L2 SSS data include a flag that indicates if a measurement of SSS is suspected of being contaminated by RFI.

Due to the significantly higher T_B of land and ice compared to ocean, difficulties with salinity retrieval are expected close to land or ice as the antenna field of view is not only of open water. A flag indicates whether L2 measurements are within 40 km of land and another flag within

200 km although studies note that there are quality issues with retrieved SSS data further from the coast than this (Reul et al., 2012).

The quality of the retrievals of SSS from space at high latitudes in the Southern Hemisphere is poor, probably as a result of one or more of the following: galactic noise (reflection of L-band radiation from the galactic plane); colder waters (lower sensitivity of T_B to changes in SSS); higher winds; and the proximity or presence of sea ice (e.g. Banks et al., 2012; Reul et al., 2012; Lagerloef et al., 2013). At high latitudes in the Northern Hemisphere, the number of retrievals has been limited by RFI (Boutin et al., 2012) and so the effects of proximity to sea ice, and so on are not as obvious.

Another reason for differences between in situ measured surface salinity and satellite salinity relates to the concept of measuring *skin* versus near-surface salinity. L-band T_B corresponds to the top ~1 cm of the ocean (Swift, 1980) whereas most in situ measurements relate to depths of a few metres (i.e. near-surface). For example, to prevent biofouling, many Argo floats switch off the pump to the conductivity-temperature cell at a pressure of between 5 and 10 db (5–10 m). However, significant differences can exist in the salinity values between skin- (~1 cm) and near-surface-depths. Reverdin, Morisset, Boutin, and Martin (2012) investigated ocean freshening between 15 and 50 cm depths in the tropical oceans and showed that, depending on wind speed and other factors, sudden drops in salinity (~0.4) can be observed related to local, heavy rainfall.

3. Data

All salinity data used here are based on ESA SMOS L2 data (processor version 5.50). For processing reasons: the climatology products are based on SMOS data from January 2010 to December 2013; daily products are over the period January 2010 through February 2015; and monthly products are from February 2010 through February 2014. Note that the monthly products are produced independently of the daily products (not by averaging the daily products) and this is computationally demanding (hence the somewhat shorter time period). Measurements were filtered according to data quality flags 25, 26 or 27 (SMOS Team, 2011); these relate to measurements identified as having issues related to convergence or geophysical/RFI problems. Data not filtered by the quality control flags can result in spurious results or returning the climatological SSS value. In addition, no L2 SSS data were included where there was land within 40 km (another SMOS flag) although further filtering based on distance to land is described later for the production of the anomaly products. Data from 2010 through 2013 inclusive are from the "catch-up" reprocessing (Font et al., 2014) that uses a consistent Ocean Target Transformation (OTT) approach, whereas data from 1 January 2014 onwards are operational (near-real time) data. Unless explicitly stated the median is used as the average to limit the potential influence of extreme values.

To demonstrate the ability of the approach in this paper to reduce the seasonal variability in ascending versus descending bias, initially three study regions were used, and these are detailed in Table 1. SPURS was based on the international Salinity Processes in the Upper Ocean Regional Study (http://spurs.jpl.nasa.gov/) in the subtropical gyre in the North Atlantic. The region selected for the subtropical South Pacific (SPac) was chosen as it lies within with the area used for SMOS calibration through the OTT (Yin et al., 2014a; OTT is computed in the 'parallelogram' defined by (121° ± 16°W at 5°S, 111° ± 16°W at 45°S) and away from any island). A third study region was selected in the SIO so that all three study regions were 30° in longitude by 20° in latitude. As well as producing the climatology and anomaly products for salinity the same methods described below have been implemented for the SST values provided in the ESA L2 product (i.e. that provided by ECMWF; SMOS Team, 2014).

Table 1
Definition of regions used in study.

Study region name (abbreviation)	Longitude range	Latitude range
Subtropical North Atlantic (SPURS)	50°W, 20 W°	15°N, 35°N
Subtropical South Pacific (SPac)	130°W, 100 W°	35°S, 15°S
Southern Indian Ocean (SInd)	75°E, 105°E	40°S, 20°S
RoSSSby	65°E, 100°E	30°S, 15°S

When it became apparent that geophysical signals, possibly Rossby waves, were observable in the SIO an additional region, named RoSSSby, was defined to investigate these signatures (Table 1; Fig. 1). The choice of RoSSSby was influenced by the studies of Rossby waves in SSS in ocean models (Heffner et al., 2008; Subrahmanyam et al., 2009) and from Aquarius (Menezes et al., 2014).

3.1. Climatology data

Climatology products are based on SMOS L2 data from 2010 through 2013 to provide daily, 1°×1° climatologies separately for ascending ($CLIM_A$) and descending ($CLIM_D$) passes using a moving window approach (in time and space). The salinity value in each one-degree grid cell is based on the average of all data remaining after applying the quality control flags (detailed above), from all four years. Spatially, the climatology for each grid cell is based on data for the grid cell as well as data from those within ±2°. Temporally, the climatology includes data from within ±4 days of the day of interest. The selection of the size of the moving window was a balance between having sufficient data and not smoothing too much in either space or time.

The daily, one-degree products can then be averaged to provide values of climatological SSS at different spatial and/or temporal resolutions — in this study we use the original daily 1°×1° data and monthly 1°×1° averages. The overall averages of $CLIM_A$ and $CLIM_D$ are shown in Fig. 1 alongside the equivalent plot from World Ocean Atlas 2013 (WOA13; Boyer et al., 2013). The latter reflects the average WOA13 climatology for the period 2005 to 2012, the WOA13 analysis period closest to the SMOS data period.

It is known that during the commissioning phase of SMOS (approximately January–June 2010) the SSS data are particularly noisy (Reul et al., 2012; Spurgeon et al., 2015) and as such may have a deleterious impact on the quality of the climatology data. However, if the data from early 2010 were not used then only three years rather than four full years of reprocessed data would have been available for building the climatology products. As the focus of this study is on demonstrating that SMOS SSS data can be used to show relatively long-period oceanographic signals it was decided to use the longest possible consistent data series and therefore to include the data from the commissioning phase.

3.2. Daily regional products

For each day in the period 20 January 2010 through 28 February 2015 values of SSS_A and SSS_D were calculated as the average of all valid measurements within each 1° cell. Only cells with at least five SSS measurements for both ascending and descending passes were included and no cell contained an ISEA grid point closer than 100 km to land. The minimum distances to land were based on the SMOS ancillary data product (SMOS Team, 2014) that details the minimum distance to land of any possible location on the ISEA grid. Using a higher threshold for distance to land results in more data being excluded, but the patterns in variability do not change substantially. To fully account for the land contamination in the SMOS SSS data a distance of greater than ~1000 km would be required (e.g. Reul et al., 2012).

3.3. Monthly anomaly data

Monthly anomaly products were produced for the period February 2010 through February 2014 inclusive. For each calendar month, all valid measurements (those meeting the requirements for the flags above) in each cell were averaged to provide SSS_A and SSS_D at monthly,

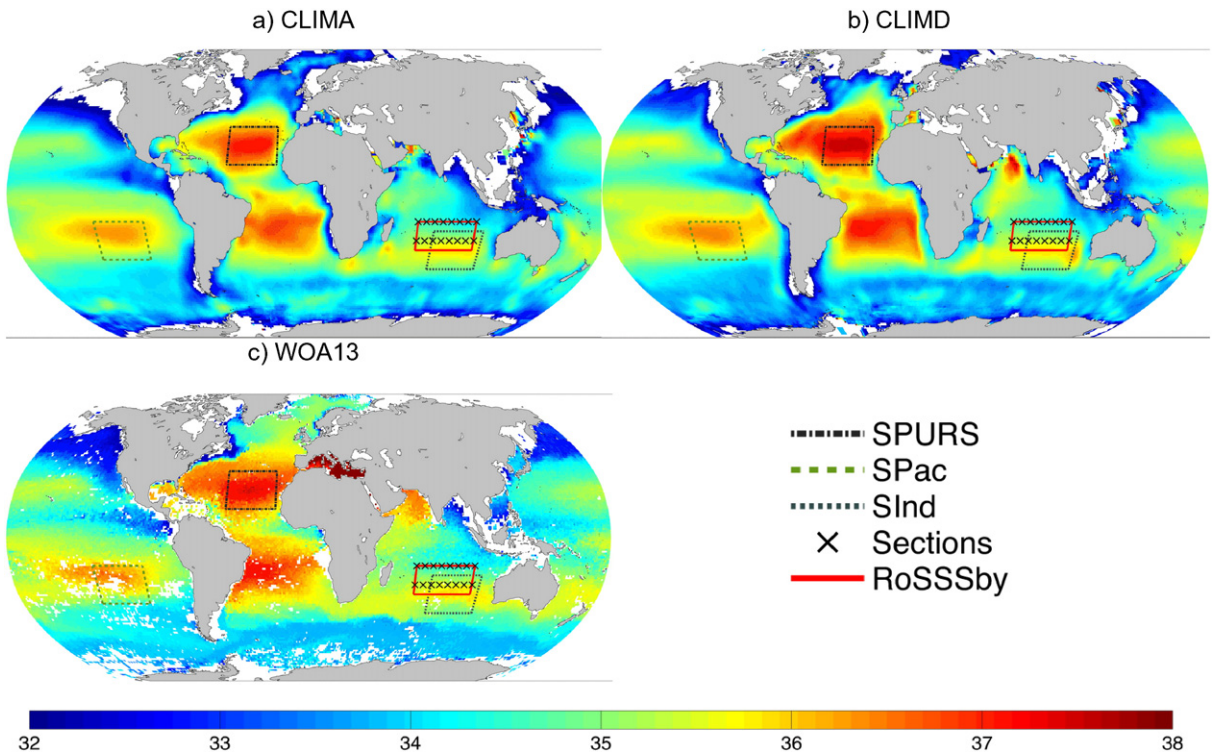

Fig. 1. Contour of annual averaged (values of daily 1° salinity with the four study regions indicated along with the sections used in Southern Indian Ocean for a) $CLIM_A$ b) $CLIM_D$, c) for comparison annual average of WOA13 monthly statistical means for 2005–2012. The maps are limited to ±80° in latitude.

1°×1° resolution. For these monthly products a minimum number of 200 measurements for each cell was imposed on SSS_A and SSS_D. Although monthly anomaly data has been produced globally, the RoSSSby region is used to illustrate the effects of the choice of threshold. Fig. 2 shows the distribution of the number of valid observations per grid cell within the RoSSSby region over all 49 months, with the threshold of 200 marked (87% of cells included for SSS_A and 82% for SSS_D). The monthly values of $ANOM_A$ and $ANOM_D$ were calculated by subtracting the climatology, although in this case the climatologies were the monthly averaged values. In addition, as with the daily products, to reduce the impact of land contamination, any cells where the minimum distance to land was less than 100 km were excluded.

3.4. Sea surface height anomaly data

For comparison purposes we used monthly maps of SSHA from the ESA CCI (Climate Change Initiative). These are global gridded (0.25° × 0.25°) anomalies of SSH with respect to the mean temporal

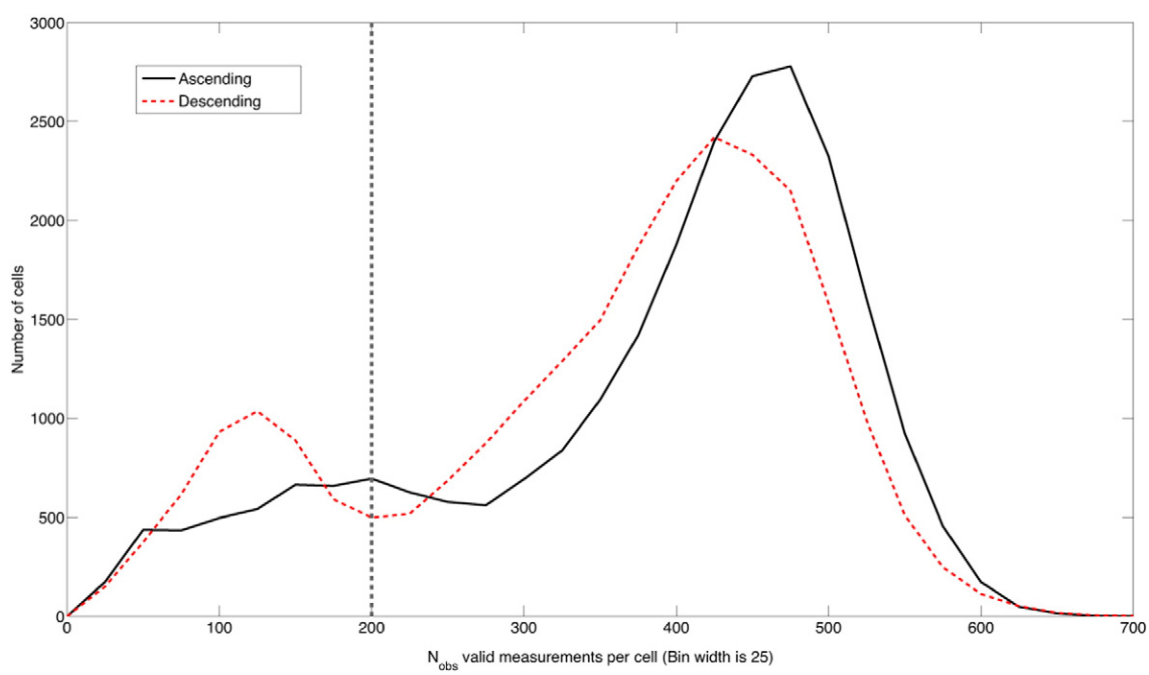

Fig. 2. Distribution of number of observations per cell over all months for RoSSSby region (30°S–15°S, 65°E–100°E) for ascending passes (solid black line) and descending passes (dashed red line). Threshold for selection of grid cells (N_{obs} = 200) shown as dashed grey line.

value (based on the DTU10 mean sea surface; see Andersen, 2010 for further details) at each location and are currently available over the period January 1993 to December 2014. This new dataset has been obtained by merging data from several available radar altimeter missions, and using carefully selected instrumental and geophysical corrections to ensure its suitability for climate research. More details on this dataset can be found in Ablain et al. (2015).

4. Method

4.1. Spatio-temporal variability of biases

To investigate the spatio-temporal nature of the ascending-descending bias, for each cell, the daily values of SSS_D were subtracted from the daily values of SSS_A (giving ΔSSS). The process was repeated to calculate the difference for daily $ANOM_A$ minus $ANOM_D$ (ΔANOM). For each of the three study regions (SPURS, SPac and SInd), the daily values of ΔSSS and ΔANOM were averaged over all cells within the study region. To verify that the methodology developed here captures any seasonally varying behaviour, the equivalent differences in daily climatology products were calculated by subtracting $CLIM_D$ from $CLIM_A$ (ΔCLIM). Any seasonally varying behaviour in all years' ΔSSS should be similar to ΔCLIM.

4.2. Feature propagation

This section is concerned with studying westward-propagating features within monthly data in the RoSSSby study area. Monthly data are used in preference to the noisier daily data to help with feature detection. Propagating features have been highlighted by filtering (see below) the longitude-time plots of SSS, SST and SSH anomalies and their speeds analysed with the Radon Transform. The same processing of anomalies has been applied to all datasets. The monthly data in time-longitude space have been filtered using a westward-propagating filter. This filter is in concept similar to the one described in O'Brien, Cipollini, and Blundell (2013), a band-pass infinite impulse response (IIR) filter passing a range of frequencies and wavenumbers in the westward-propagating quadrants only of the 2-D Fourier Transform of the longitude-time plot. In this study we aim at demonstrating concurrent (i.e. coexisting, but not necessarily in phase) westward-propagating signals, without making assumptions on their wavenumber and frequency. Therefore the filter passband has been widened to encompass the entire westward-propagating quadrants, i.e. making it a westward all-pass. Note that the filter mask still excludes the frequency and wavenumber axes, i.e. the filter rejects any signals stationary in time (zero-frequency) and/or space (zero-wavenumber).

An objective estimate of the propagation speeds has then been obtained by applying the Radon Transform to the longitude-time plot, as explained by Cipollini, Quartly, Challenor, Cromwell, and Robinson (2006), using the whole longitude span of 35° [65°E to 100°E] and removing the mean value of the longitude-time plot prior to the analysis, as suggested by de la Rosa, Cipollini, and Snaith (2007). The same processing of anomalies ($ANOM_A$ and $ANOM_D$) has been applied to salinity (SSS_A and SSS_D), SST (anomaly from ascending passes and anomaly from descending passes) and SSHA data.

5. Results and discussion

5.1. Climatology products

The average (over all days) climatology products for $CLIM_A$ and $CLIM_D$ are shown in Fig. 1 alongside the equivalent results for WOA13 (median over all months). The synoptic results from SMOS are generally in good agreement with the results from WOA13 (e.g. Atlantic more saline than Pacific, subtropical gyres in correct locations). However, there are significant differences at high latitudes and in coastal regions, as discussed in Section 2.1.2. Other areas also show differences amongst the three products, for example, a high salinity region in the eastern portion of SInd can be observed for $CLIM_D$ but not for WOA13 or $CLIM_A$. However, due to the spatio-temporal variability of both the ascending/descending bias and the number of valid SSS values care should be taken when interpreting such features as oceanographic rather than artefacts of the processing. Note that WOA13 refers to the period 2005–2012 and so there are regions where no data have been collected in this relatively short period.

5.2. Spatio-temporal variability of bias

For each of the three study regions, the values of daily average ΔSSS are shown by day of year in Fig. 3 with the different colours indicating the different years (2010–2015). If there were no difference between data from ascending passes and data from descending passes then ΔSSS would be zero, as the diurnal variability (due to the 12 h difference in ascending and descending passes) on these spatio-temporal scales is small (Zhang & Zhang, 2012). The equivalent differences between $CLIM_A$ and $CLIM_D$ are also shown for each region and these show the average annual cycle. Not unexpectedly, all three study regions show higher frequency variability around the climatological signals. In particular, the SPURS region shows a marked repeating annual cycle. The amplitudes of the annual cycles in SPac and SInd are lower than that for the SPURS region.

During the (boreal) late autumn and winter there are a limited number of valid measurements of SSS_D in the SPURS region (Fig. 4) and this is a possible cause of the variability between the individual years (2010 in particular) from the climatological values (approximately from start of year to day 50 and from day 245 to end of year in Fig. 3). Hernandez et al. (2014) noted that during boreal winter in a similar location large biases are present possibly due to strong Sun. contamination on descending orbits at that time (see also Spurgeon et al., 2015). Both SPac and SInd show a marked deviation in ΔSSS from zero over the period between (approximately) days 220 to 320: this may be as a result of noise from galactic glint reported in descending passes in September–October within 30° of the equator (Spurgeon et al., 2015).

Descriptive statistics for ΔSSS and ΔANOM for the three study regions are given in Table 2. In all cases, the magnitudes of both the mean and the standard deviation of ΔANOM are less than for those for ΔSSS. In SPURS and SPac the medians for ΔANOM are less in absolute value than the medians for ΔSSS but this is not the case in SInd although both medians are close to zero. As such it is concluded that ΔANOM reduces the bias relative to ΔSSS.

5.3. Feature propagation

In order to establish whether the anomaly products produced in this study show plausible oceanographic signals, the temporal evolution of the signals is considered in the RoSSSby area within the SIO. A region of the SIO between 15°S–30°S and 65°–100°E was selected as intense westward propagation due to eddies (especially poleward of 20°S, Chelton et al., 2011b), and planetary waves (O'Brien et al., 2013) has been reported in this area.

Fig. 5 shows examples of the longitude-time plots for the RoSSSby region for SSS_A, $ANOM_A$, SST anomaly from ascending passes and SSHA at 15°S and 25°S. The data have been processed as described in Section 4.2 and the plots show SMOS data from ascending passes for salinity and temperature; plots from descending passes show similar results but are not shown here. The plots visually show westward propagating anomalies of similar speeds in the three anomaly datasets; the speeds at 25°S are slower than at 15°S. An objective estimate of the speeds has been carried out over the three anomaly datasets, separately for the ascending and descending data for SSS and SST, at every 1° latitude between 15°S and 30°S with the Radon Transform technique. The estimated speeds are shown as a function of latitude in Fig. 6, which

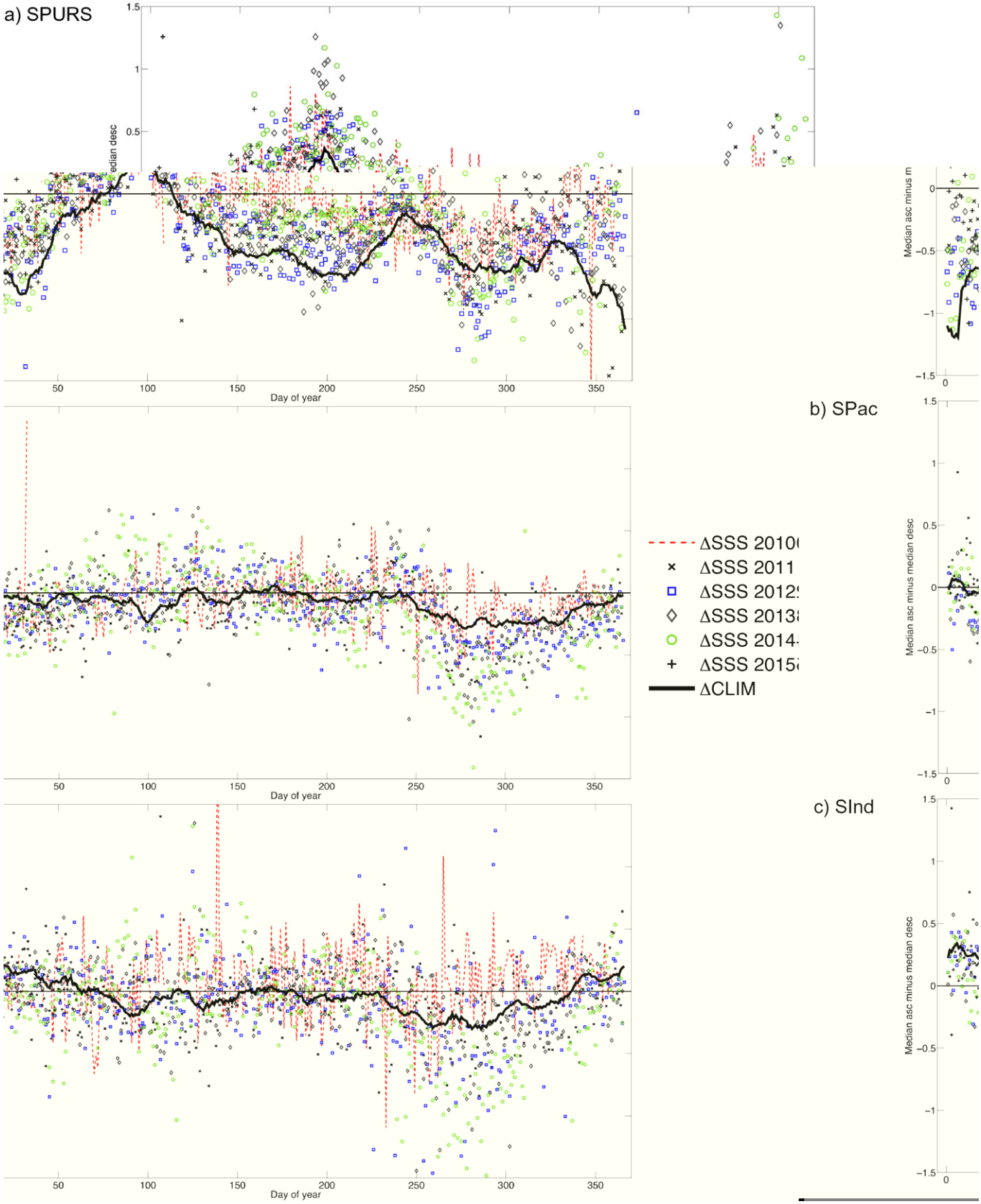

Fig. 3. Average, daily ascending minus descending SSS (ΔSSS) against day of year for the period 20 January 2010–28 February 2015 for a) SPURS, b) SPac and c) SInd. The solid-black line shows the same for ΔCLIM. Y-axis truncated at ±1.5 (only of relevance to a small number of outliers in all three regions).

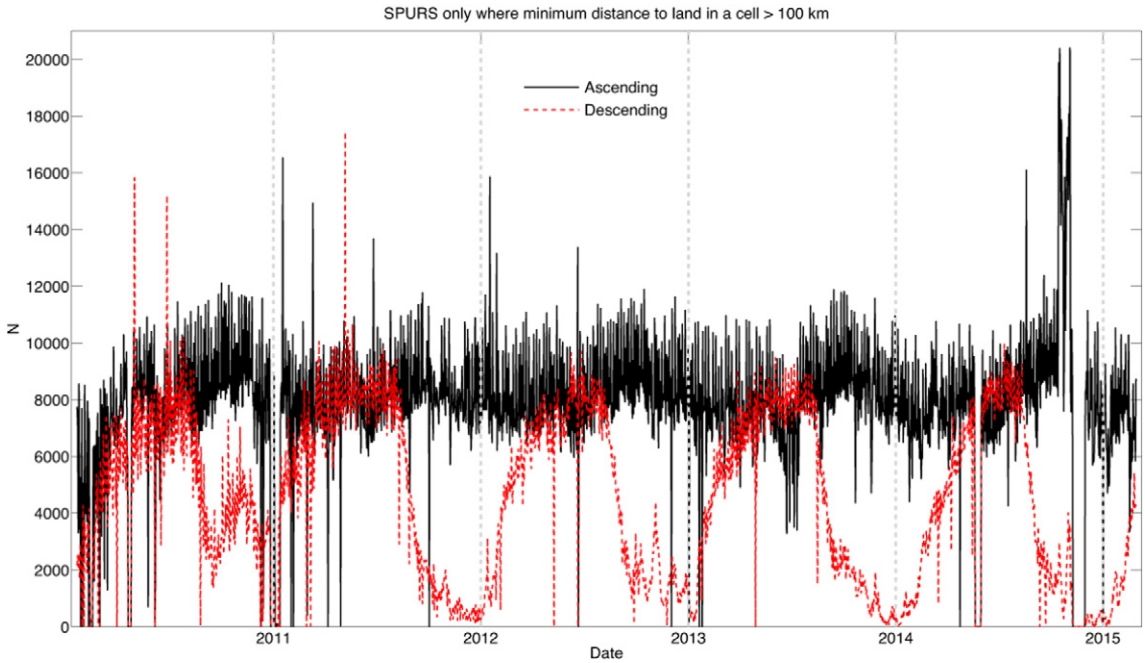

Fig. 4. Number of valid L2 SMOS measurements in SPURS region by day for ascending passes (solid black line) and descending passes (dashed red line) for period 20 January 2010 through 28 February 2015. Dashed grey lines show 1 January.

also shows the theoretical speeds for the 1st, 2nd and 3rd baroclinic modes of planetary wave propagation based on the extended theory of Killworth and Blundell (2003a, 2003b) but recomputed using WOA13 climatological data for the period 2005 to 2012. It is worth noting that there are no substantive differences in the theoretical speeds based on the ~7 years of data for WOA13 compared to the entire World Ocean Atlas 2009 dataset (Antonov et al., 2009). At 25°S, the annual gaps in the first half of the year for SSS_A and $ANOM_A$ (Fig. 5b) are most likely a result of galactic noise in ascending passes (Spurgeon et al., 2015): similar gaps for the same reason are not expected at 15°S and this is the case in Fig. 5a.

At a number of latitudes the results from the automated Radon transform algorithm show multiple peaks of the Radon Transform variance as a function of angle, indicating a superposition of signals propagating at different speeds (for a full discussion of this issue see Maharaj, Holbrook, & Cipollini, 2009); by default the method returns the speed based on the first (largest) peak. In a few locations this speed is significantly different from the speed expected for first- or second-mode baroclinic Rossby waves, but there is a second- or third-largest peak whose speed is much more consistent with what expected from theory and with speeds from adjoining latitudes. For $ANOM_A$ this happens at 30°S, where the largest-peak speed was 2.5 cm/s while the second was 1.0 cm/s, and the third, which we have selected, is at 4.0 cm/s. For $ANOM_D$, there are a number of such latitudes; these are 16°S (first peak speed 3.6 cm/s, second peak at 10.5 cm/s), 29°S (8.3 cm/s, second peak at 4.2 cm/s) and 30°S (5.6 cm/s, second peak at 4.7 cm/s). The results for $ANOM_A$ and $ANOM_D$ are shown in Fig. 6. A similar 'peak selection' approach on the anomalies from SST at 15°S would result in increased speeds of 15.2 cm/s and 11.2 cm/s for ascending and descending data respectively (not shown in Fig. 6).

The propagation speeds identified from the above approach are shown in Fig. 5 at 15°S and 25°S for the three anomaly variables. As discussed above, the second peak was identified as the speed for SST anomaly at 15°S and this is shown as the dotted line whereas the first peak (dashed line at 3.9 cm/s) is shown as the dashed line. As can be seen in Fig. 5b for ascending passes and Fig. 6 (ascending and descending passes) the speeds at 25°S for SST anomaly are less than those from SSHA or $ANOM_A$. For SST anomaly at 25°S (Fig. 5b) the dotted line represents the second peak in the Radon transform (a speed of 6.9 cm/s rather than the dashed line at 3.3 cm/s). The higher speed can be seen to be in better agreement with results for SSHA and SSS anomalies (Fig. 5 and Fig. 6).

At the southern end of the study region the observed speeds in all three datasets ($ANOM_A$, $ANOM_D$ and SSHA) agree well with the mode 1 theoretical speeds for Rossby waves, while north of 27°S they are in between the speeds for the first and second modes. Values are very similar to those found globally by O′Brien et al. for co-propagating features in chlorophyll, SSHA and SST (see Fig. 5 in O'Brien et al., 2013) with dominant wavelengths in the range 600–800 km. These could be either large eddies or planetary waves, but the precise attribution of those signal to one class of phenomena or the other goes beyond the scope of this work. Likewise, the mechanisms responsible for the generation of a signature in the SSS dataset should be investigated by looking at the phase relationship of the co-propagating signals, as described by Killworth et al. (2004) for the SSHA-chlorophyll case and also applied by O'Brien et al. (2013) for the chlorophyll-SSHA-SST case. This is deferred to a future paper.

The magnitudes of $ANOM_A$ and $ANOM_D$ are of the same order of magnitude as the SSS anomalies in Menezes et al. (2014). However, the methodology in this study was designed to investigate whether the zonal (and westward-filtered) signal was in line with prediction of planetary waves/eddies. As such the speeds identified here represent only one component, and therefore cannot be compared directly, with the velocities identified in the empirical approach of Menezes et al. as the latter identifies the predominant 2-D (i.e. with both zonal and meridional components) mode of propagation with a Complex Empirical Orthogonal Function analysis.

Table 2
Comparison of descriptive statistics for ΔSSS and ΔANOM by study region (pss).

	Mean		Standard deviation		Median	
	ΔSSS	ΔANOM	ΔSSS	ΔANOM	ΔSSS	ΔANOM
SPURS	−0.206	0.137	0.403	0.331	−0.224	0.123
SPac	−0.116	−0.033	0.284	0.236	−0.100	−0.031
SInd	−0.052	−0.034	0.364	0.324	−0.023	−0.032

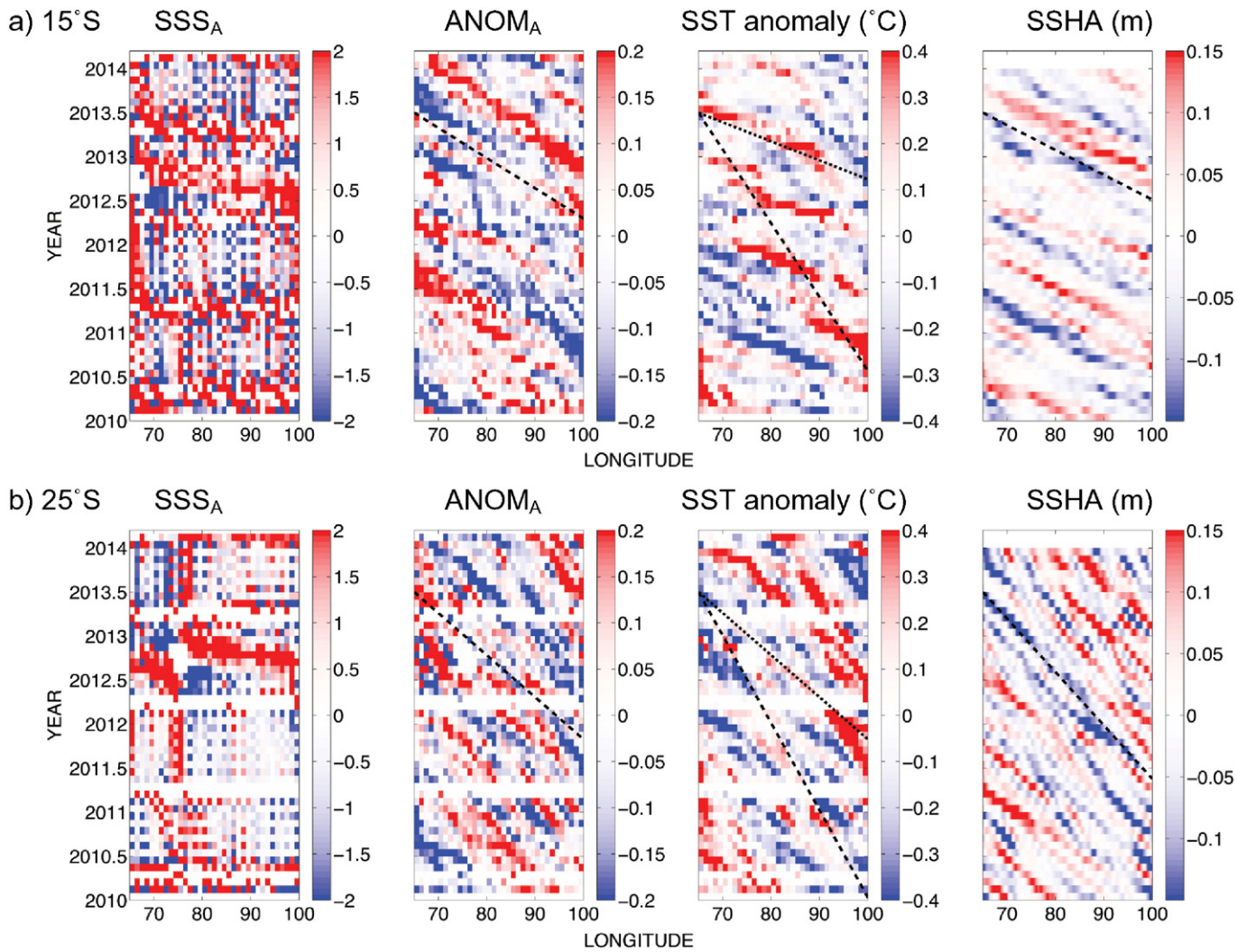

Fig. 5. Longitude-time plots of monthly anomalies for, from left, SSS_A (pss), $ANOM_A$ (pss) and SST anomaly from ascending passes (°C) and SSHA (m) during the period February 2010–February 2014 between 65°–100°E at a) 15°S and b) 25°S. Data have been filtered as described in text. The dashed black lines show the Rossby wave propagation speed based on the Radon Transform (first peak). Dotted lines for SST anomaly are the speeds from the second peak of the Radon transform.

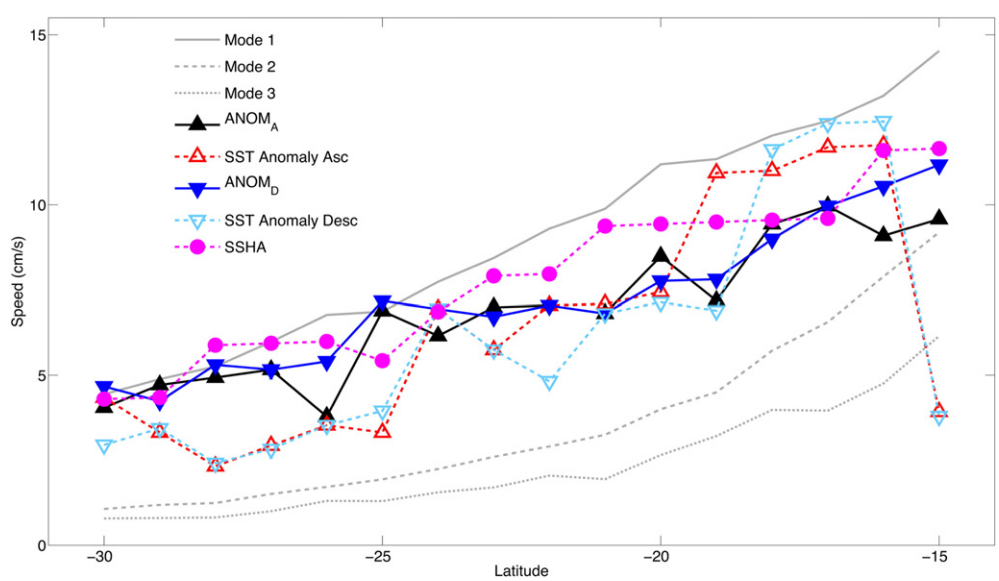

Fig. 6. Speed of westward propagating features from $ANOM_A$ (solid, black upward pointing triangle); $ANOM_D$ (solid, blue downward pointing triangle); SST anomaly from ascending passes (red, upward pointing triangle); SST anomaly from descending passes (light blue, downward pointing triangle); SSHA (solid, magenta circle). The grey lines are the theoretical speeds for the 1st (solid), 2nd (dashed) and 3rd (dotted) baroclinic mode of planetary wave propagation based on the extended theory of Killworth and Blundell (2003a, 2003b) recomputed using WOA13.

6. Conclusions

It has been shown that ESA Level 2 SSS data contain biases between data from ascending passes and data from descending passes that vary both in space and time. Using three study regions (SPURS, SInd and SPac) we have demonstrated that these strong seasonally varying signals can be significantly reduced in magnitude in the open ocean through the use of SMOS climatology products to build SSS anomalies (Table 2). For all three study regions the mean and standard deviation of the difference between ascending and descending passes is reduced for ΔANOM compared to ΔSSS. One disadvantage of the anomaly approach is that calibration of the anomaly values to reflect an absolute value of salinity would require adjustment to some reference salinity.

The study includes near-real time data as well as data from the catch-up reprocessing where the latter is known to be of better quality. In addition, noisy data from the commissioning phase of SMOS has been included. Although limiting the study to only the higher quality data (reprocessed and from after June 2010, i.e. June 2010–December 2013) may result in enhanced results the record length would be reduced to less than four years, which may be insufficient to study longer term features. In addition, any studies concerned with the operational assimilation of SMOS anomalies would not be possible.

Geophysical signals are clearly visible within the anomaly products for salinity, temperature and the independent sea surface height data. As an example, we have shown the propagation speed of westward moving features in the RoSSSby region of the SIO is consistent amongst the datasets (Fig. 6) and with previously published results on large-scale non-linear eddies/Rossby waves in the SIO. Such features are not clearly discernible in equivalent plots for SSS_A (Fig. 5) or SSS_D (not shown).

Acknowledgements

This work was supported by the ESA STSE SMOS+SOS Project (http://smos-sos.org/) and NERC National Capability via National Centre for Earth Observation (http://www.nceo.ac.uk/) and National Oceanography Centre (http://www.noc.ac.uk). The authors are grateful to Paul Spurgeon of Argans Ltd., UK for his advice on SMOS data products and to the two anonymous reviewers for their helpful suggestions.

References

Ablain, M., Cazenave, A., Larnicol, G., Balmaseda, M., Cipollini, P., Faugere, Y., ... Benveniste, J. (2015). Improved sea level record over the satellite altimetry era (1993–2010) from the climate change initiative project. *Ocean Science*, *11*, 67–82.

Andersen, O. B. (2010). The DTU10 gravity field and mean sea surface. *Second International Symposium of the Gravity Field of the Earth (IGFS2)*. Alaska, USA: Fairbanks.

Antonov, J. I., Seidov, D., Boyer, T. P., Locarnini, R. A., Mishonov, A. V., Garcia, H. E., ... Johnson, D. R. (2009). World Ocean Atlas 2009, volume 2: Salinity. In S. Levitus (Ed.), *NOAA Atlas NESDIS 69 World Ocean Atlas 2009*. Washington D.C., USA: NOAA (184 pp.).

Banks, C. J., Gommenginger, C. P., Srokosz, M. A., & Snaith, H. M. (2012). Validating SMOS ocean surface salinity in the Atlantic with argo and operational ocean model data. *IEEE Transactions on Geoscience and Remote Sensing*, *50*, 1688–1702.

Boutin, J., Martin, N., Yin, X. B., Font, J., Reul, N., & Spurgeon, P. (2012). First assessment of SMOS data over open ocean: Part II—Sea surface salinity. *IEEE Transactions on Geoscience and Remote Sensing*, *50*, 1662–1675.

Boutin, J., Martin, N., Reverdin, G., Morisset, S., Yin, X., Centurioni, L., & Reul, N. (2014). Sea surface salinity under rain cells: SMOS satellite and in situ drifters observations. *Journal of Geophysical Research, Oceans*, *119*, 5533–5545.

Boyer, T., Mishonov, A. (Technical Ed.) (2013). World Ocean Atlas 2013 Product Documentation (http://www.nodc.noaa.gov/OC5/indprod.html). In T. Boyer, Mishonov, A. (Technical Ed.) (Ed.).

Brown, M. A., Torres, F., Corbella, I., & Colliander, A. (2008). SMOS calibration. *IEEE Transactions on Geoscience and Remote Sensing*, *46*, 646–658.

Chelton, D. B., & Schlax, M. G. (1996). Global observations of oceanic Rossby waves. *Science*, *272*, 234–238.

Chelton, D. B., Gaube, P., Schlax, M. G., Early, J. J., & Samelson, R. M. (2011a). The influence of nonlinear mesoscale eddies on near-surface oceanic chlorophyll. *Science*, *334*, 328–332.

Chelton, D. B., Schlax, M. G., & Samelson, R. M. (2011b). Global observations of nonlinear mesoscale eddies. *Progress in Oceanography*, *91*, 167–216.

Cipollini, P., Cromwell, D., Challenor, P. G., & Raffaglio, S. (2001). Rossby waves detected in global ocean colour data. *Geophysical Research Letters*, *28*, 323–326.

Cipollini, P., Quartly, G. D., Challenor, P. G., Cromwell, D., & Robinson, I. S. (2006). Remote sensing of extra-equatorial planetary waves. In A. B. Rencz, & J. F. R. Gower (Eds.), *Manual of remote sensing, volume 6: Remote sensing of marine environment* (pp. 61–68). Bethesda MD, USA: American Society for Photogrammetry and Remote Sensing.

de la Rosa, S., Cipollini, P., & Snaith, H. M. (2007). An application of the radon transform to study planetary waves in the Indian Ocean. *Envisat Symposium 2007*. Montreux: ESA.

ESA Earth Observation Programme Board (2011). *SMOS (EOEP) Quarterly Status Report July–September 2011 (QSR 2011/3)*. Paris, France: European Space Agency.

Font, J., Boutin, J., Reul, N., Spurgeon, P., Arias, M., Gabarró, C., ... Delwart, S. (2014). Read-me-first note for SMOS level 2 sea surface salinity (SSS) data products. https://earth.esa.int//documents/10174/127856/SMOS_Level-2_Ocean_Salinity_RN

Fournier, S., Chapron, B., Salisbury, J., Vandemark, D., & Reul, N. (2015). Comparison of spaceborne measurements of sea surface salinity and colored detrital matter in the Amazon plume. *Journal of Geophysical Research, Oceans*, *120*, 3177–3192.

GCOS (2011). GCOS ocean surface ECV sea surface salinity (SSS). http://gosic.org/content/gcos-oceanic-surface-ecv-sea-surface-salinity

Gould, J., Roemmich, D., Wijffels, S., Freeland, H., Ignaszewsky, M., Jianping, X., ... Riser, S. (2004). Argo profiling floats bring new era of in situ ocean observations. *EOS Trans*, *85*(19).

Grodsky, S. A., Reul, N., Lagerloef, G., Reverdin, G., Carton, J. A., Chapron, B., ... Kao, H. Y. (2012). Haline hurricane wake in the Amazon/Orinoco plume: AQUARIUS/SACD and SMOS observations. *Geophysical Research Letters*, *39*.

Heffner, D. M., Subrahmanyam, B., & Shriver, J. F. (2008). Indian Ocean Rossby waves detected in HYCOM sea surface salinity. *Geophysical Research Letters*, *35*.

Hernandez, O., Boutin, J., Kolodziejczyk, N., Reverdin, G., Martin, N., Gaillard, F., ... Vergely, J. L. (2014). SMOS salinity in the subtropical North Atlantic salinity maximum: 1. Comparison with Aquarius and in situ salinity. *Journal of Geophysical Research, Oceans*, *119*, 8878–8896.

Hill, K. L., Robinson, I. S., & Cipollini, P. (2000). Propagation characteristics of extratropical planetary waves observed in the ATSR global sea surface temperature record. *Journal of Geophysical Research, Oceans*, *105*, 21927–21945.

Killworth, P. D., & Blundell, J. R. (2003a). Long extratropical planetary wave propagation in the presence of slowly varying mean flow and bottom topography. Part I: The local problem. *Journal of Physical Oceanography*, *33*, 784–801.

Killworth, P. D., & Blundell, J. R. (2003b). Long extratropical planetary wave propagation in the presence of slowly varying mean flow and bottom topography. Part II: Ray propagation and comparison with observations. *Journal of Physical Oceanography*, *33*, 802–821.

Killworth, P. D., Chelton, D. B., & DeSzoeke, R. A. (1997). The speed of observed and theoretical long extratropical planetary waves. *Journal of Physical Oceanography*, *27*, 1946–1966.

Killworth, P. D., Cipollini, P., Uz, B. M., & Blundell, J. R. (2004). Physical and biological mechanisms for planetary waves observed in satellite-derived chlorophyll. *Journal of Geophysical Research, Oceans*, *109*.

Lagerloef, G., Kao, H., & Aquarius Cal/Val Team (2013). Aquarius data release V2.0 validation analysis: Analysis period: Sep 2011–Dec 2012. *SMOS & Aquarius Science Workshop*. France: Brest.

Lagerloef, G., Kao, H.-Y., Meissner, T., & Vazquez, J. (2015). Aquarius salinity validation analysis; data version 4.0. In: ftp://podaac-ftp.jpl.nasa.gov/allData/aquarius/docs/v4/AQ-014-PS-0016_AquariusSalinityDataValidationAnalysis_DatasetVersion4.0and3.0.pdf.

Maharaj, A. M., Holbrook, N. J., & Cipollini, P. (2009). Multiple westward propagating signals in South Pacific sea level anomalies. *Journal of Geophysical Research, Oceans*, *114*.

Mecklenburg, S., Drusch, M., Kerr, Y. H., Font, J., Martin-Neira, M., Delwart, S., ... Crapolicchio, R. (2012). ESA's soil moisture and ocean salinity mission: Mission performance and operations. *IEEE Transactions on Geoscience and Remote Sensing*, *50*, 1354–1366.

Menezes, V. V., Vianna, M. L., & Phillips, H. E. (2014). Aquarius sea surface salinity in the South Indian Ocean: Revealing annual-period planetary waves. *Journal of Geophysical Research, Oceans*, *119*, 3883–3908.

O'Brien, R. C., Cipollini, P., & Blundell, J. R. (2013). Manifestation of oceanic Rossby waves in long-term multiparametric satellite datasets. *Remote Sensing of Environment*, *129*, 111–121.

Oliva, R., Nieto, S., & Felix-Redondo, F. (2013). RFI detection algorithm: Accurate geolocation of the interfering sources in SMOS images. *Geoscience and Remote Sensing, IEEE Transactions on*, *51*, 4993–4998.

Reul, N., Tenerelli, J., Boutin, J., Chapron, B., Paul, F., Brion, E., ... Archer, O. (2012). Overview of the first SMOS Sea surface salinity products. Part I: Quality assessment for the second half of 2010. *IEEE Transactions on Geoscience and Remote Sensing*, *50*, 1636–1647.

Reul, N., Chapron, B., Lee, T., Donlon, C., Boutin, J., & Alory, G. (2014). Sea surface salinity structure of the meandering Gulf Stream revealed by SMOS sensor. *Geophysical Research Letters*, *41*, 3141–3148.

Reverdin, G., Morisset, S., Boutin, J., & Martin, N. (2012). Rain-induced variability of near sea-surface T and S from drifter data. *Journal of Geophysical Research*, *117*, C02032.

SMOS Team (2010). SMOS L2 OS AlgorithmTheoretical Baseline Document. (http://www.argans.co.uk/smos/docs/deliverables/delivered/ATBD/SO-TN-ARG-GS-0007_L2OS-ATBD_v3.6_101207.pdf). *ARGANS/ACRI-st, ICM-CSIC, LOCEAN/SA/CETP, IFREMER*.

SMOS Team (2011). SMOS L2 OS input/output data definition (http://www.argans.co.uk/smos/docs/deliverables/delivered/IODD/SO-TN-ARG-GS-0009_L2OS-IODD_v2.20_111117.pdf). *Argans, ICM-CSIC, LOCEAN/SA/CETP, IFREMER*.

SMOS Team (2014). SMOS L2 OS input/output data definition. (http://www.argans.co.uk/smos/docs/deliverables/delivered/IODD/SO-TN-ARG-GS-0009_L2OS-IODD_v2.25_140905.pdf). *ARGANS/ACRI-st, ICM-CSIC, LOCEAN/SA/CETP, IFREMER*.

Soldo, Y., Khazaal, A., Cabot, F., Richaume, P., Anterrieu, E., & Kerr, Y. H. (2014). Mitigation of RFIS for SMOS: A distributed approach. *Geoscience and Remote Sensing, IEEE Transactions on*, *52*, 7470–7479.

Spurgeon, P., Arias, M., Font, J., Turiel, A., Olmedo, E., Portabella, M., ... Vergely, J. T. -L. (2015). Five years of SMOS ocean salinity: Selecting data. *2nd SMOS Science Conference*. ESAC.

Subrahmanyam, B., Heffner, D. M., Cromwell, D., & Shriver, J. F. (2009). Detection of Rossby waves in multi-parameters in multi-mission satellite observations and HYCOM simulations in the Indian Ocean. *Remote Sensing of Environment*, *113*, 1293–1303.

Suess, M., Matos, P., Gutierrez, A., Zundo, M., & Martin-Neira, M. (2004). Processing of SMOS level 1C data onto a Discrete Global Grid. *IGARSS 2004: IEEE International Geoscience and Remote Sensing Symposium Proceedings, Vols 1–7 — Science for Society: Exploring and Managing a Changing Planet* (pp. 1914–1917). New York: IEEE.

Swift, C. T. (1980). Passive microwave remote-sensing of the ocean - review. *Boundary-Layer Meteorology*, *18*, 25–54.

Tenerelli, J. E., Reul, N., Mouche, A. A., & Chapron, B. (2008). Earth-viewing L-band radiometer sensing of sea surface scattered celestial sky radiation — Part I: General characteristics. *IEEE Transactions on Geoscience and Remote Sensing*, *46*, 659–674.

Tzortzi, E., Josey, S. A., Srokosz, M., & Gommenginger, C. (2013). Tropical Atlantic salinity variability: New insights from SMOS. *Geophysical Research Letters*, *40*, 2143–2147.

Wentz, F. J., & Le Vine, D. M. (2011). Algorithm theoretical basis document: Aquarius salinity retrieval algorithm: Final pre-launch version. (http://oceancolor.gsfc.nasa.gov/AQUARIUS/DOCS/Level2_salinity_atbd_final_prelaunch.pdf). *RSS Technical Report 011811*.

Yin, X., Boutin, J., Martin, N., Spurgeon, P., Vergely, J. -L., & Gaillard, F. (2014a). Errors in SMOS sea surface salinity and their dependency on a priori wind speed. *Remote Sensing of Environment*, *146*, 159–171.

Yin, X. B., Boutin, J., Reverdin, G., Lee, T., Arnault, S., & Martin, N. (2014b). SMOS sea surface salinity signals of tropical instability waves. *Journal of Geophysical Research, Oceans*, *119*, 7811–7826.

Yueh, S. H. (1997). Modeling of wind direction signals in polarimetric sea surface brightness temperatures. *IEEE Transactions on Geoscience and Remote Sensing*, *35*, 1400–1418.

Yueh, S. (2013). Aquarius CAP algorithm and data user guide V2.0. In. ftp://podaac-ftp.jpl.nasa.gov/allData/aquarius/docs/CAPv2/Aquarius-CAP-User-Guide-v2.0.pdf.

Yueh, S. H., Tang, W., Fore, A. G., Neumann, G., Hayashi, A., Freedman, A., ... Lagerloef, G. S. E. (2013). L-band passive and active microwave geophysical model functions of ocean surface winds and applications to Aquarius retrieval. *IEEE Transactions on Geoscience and Remote Sensing*, *51*, 4619–4632.

Zhang, Y., & Zhang, X. (2012). Ocean haline skin layer and turbulent surface convections. *Journal of Geophysical Research, Oceans*, *117*.